Dislocation dissociation assisted formation mechanism of sigma phase and its impact on producing heterogeneous lamellar microstructure in CoCrV medium-entropy alloy

Luda Wang [a,b,d], Hai-Le Yan [a,*], Yudong Zhang [b,d,*], Benoit Beausir [b,d], Weimin Gan [c], Peltier Laurent [b], Nathalie Siredey-Schwaller [b], Claude Esling [b], Xiang Zhao [a], Liang Zuo [a]

[a] *Key Laboratory for Anisotropy and Texture of Materials, Ministry of Education, Northeastern University, Shenyang 110819, China*
[b] *Université de Lorraine, CNRS, Arts et Metiers ParisTech, LEM3, Metz, France*
[c] *German Engineering Materials Science Center at MLZ. Helmholtz-Zentrum hereon, Garching, Germany*
[d] *Laboratory of Excellence on Design of Alloys for low-mAss Structures (DAMAS), Université de Lorraine, Metz, France*

ARTICLE INFO

ABSTRACT

Control of topologically close-packed sigma phase, meaning limiting its massive presence to avoid embrittlement but benefiting its refinement and strengthening effect, is of particular interest. In-depth knowledge of dislocation-associated formation mechanisms is needed but not well addressed. In this work, an FCC-phased $Co_{66.66}Cr_{16.67}V_{16.67}$ medium entropy alloy (MEA) with a propensity to form the sigma phase at non-equilibrium conditions was studied. The alloy was conventionally cold-rolled and heat-treated. The dislocation activity rooted formation mechanisms of the sigma phase were thoroughly characterized and evidenced by *in-situ* and *ex-situ* multi-scale diffraction techniques. It was revealed that nano-sized sigma particles enriched in Cr and V and depleted in Co were precipitated ultra-rapidly and uniquely during the heating process after the cold-rolling. The precipitation is spatially inhomogeneous, mainly in the severely deformed regions. The ultra-rapidity of the precipitation was achieved by the segregation of the Cr and V atoms via crystal defect-aided diffusion for composition change and by structure transformation via dislocation dissociation. The similarity of the atomic arrangement of the partial dislocations to that of the {001} sigma planes provides favorable structure transformation stimulus. In consequence, the orientations of the intensively activated dislocation slip planes dictated those of the sigma {001} planes via the FCC {111} to sigma {001} heredity, leading to the specific sigma texture. Owing to the spatially inhomogeneous precipitation, a heterogeneous lamellar microstructure was formed, composed of alternatively distributed fine dual-phased layers and coarse single-phased layers. This work provides comprehensive information on the dislocation-dissociation-assisted formation mechanism of sigma phase.

---

* Corresponding authors.
E-mail addresses: yanhaile@mail.neu.edu.cn (H.-L. Yan), yudong.zhang@univ-lorraine.fr (Y. Zhang).

1. Introduction

As a major product of crystal plasticity in metallic materials, crystal defects, especially dislocations, have shown profound influences on certain thermally induced metallurgical processes, such as crystal restoration (recovery and recrystallization) (Hunter et al., 2022; Liu et al., 1992; Sakai et al., 2014; Sakai and Ohashi, 1990) and phase transformation (Fujita and Ueda, 1972; Shen et al., 2021; Zhang et al., 2020b, 2022), demonstrating strong microstructure and mechanical property regulating capacity. For the former, the activities of the defects are majorly driven by the restoration of crystal perfectiveness, and this subject has been intensively and systematically studied by experimental characterization and theoretical modelling (Gourdet and Montheillet, 2003; Li et al., 2023; Raabe, 2014; Son and Hyun, 2022). However, for the latter, especially for the precipitation of thermodynamically non-equilibrium secondary phases, the effects of defect activities are more versatile and complicated, depending on the nature of the transformation or precipitation, i.e., displacive or diffusive. The defect activities are more unique and indispensable when the precipitation is diffusive and involves only substitutional elements with a structure change from a simple solid solution to a complex topologically close-packed intermetallic (Yang et al., 2024; Lu et al., 2023). In such cases, the different phase constituents possess quite different mechanical properties. The matrix phase should be soft and ductile, and the precipitates are hard and brittle. If the quantity, size and distribution of brittle precipitates could be properly regulated, the alloy could be endowed with much-enhanced mechanical performances benefitting only the positive contributions of the two. Thus, the study on the effect of defects that are created by cold working on the structural transformation mechanisms of the precipitation upon thermal treatment is of particular significance in practical application and in theoretical modeling.

One of the above-mentioned precipitations is the formation of the topologically close-packed tetragonal sigma phase that is typical in Cr-containing alloys, such as the high Cr steels, superalloys, duplex stainless steels (DSSs) and recently found also in Cr-containing high entropy or medium entropy alloys (HEAs and MEAs) (Laplanche et al., 2018; Liu et al., 2016, 2024; Lu et al., 2023; Schwind et al., 2000; Tsai et al., 2013b). Due to its intrinsic hardness and brittleness, its massive presence results in a significant loss of room temperature ductility (Li and Li, 2020; Ming et al., 2017). Thus, the formation of the sigma phase has turned out to be a major concern in the recently developed HEAs and MEAs. Studying its formation criteria has become a practical and also attractive issue.

So far, it has been revealed that for the HEAs and MEAs the sigma phase is generally formed with two groups of transition elements, one being group VB-VIIB and the other group VIIB-VIIIB elements with equiatomic ratio (Joubert, 2008; Tsai et al., 2013a). The formation of the sigma phase is closely related to the specific atomic properties of the constituent elements that are the valence electron concentration (VEC) (Tsai et al., 2013a), the paired sigma-forming element (PSFE) (Tsai et al., 2016) (the equiatomic quantities that the two groups of sigma-forming elements can be obtained from the matrix), the Pauling electronegativity difference of the constituent elements in the matrix $\Delta\chi$ (Dong et al., 2014) and the lattice distortion caused by atomic radius difference δr_i (i is the i_{th} constituent element of the matrix) (Senkov and Miracle, 2003). These criteria worked well individually or synergistically, significantly advancing our understanding of sigma formation in HEAs and MEAs. However, the established criteria have solely taken into consideration of the atomic contributions of the constituent elements and under defect-free and compositional equilibrium state, which is much more useful for alloy design aiming at eliminating sigma formation to avoid its harmful mechanical influence.

On the contrary to the harmful effect, the positive contribution of the sigma phase to the formation of the heterogeneous microstructures was also discovered. Some recent examinations (Chen et al., 2023; He et al., 2021; Lu et al., 2023) have demonstrated that if the size and distribution of the sigma particles could be appropriately controlled, the presence of the sigma particles could bring beneficial influences on the overall mechanical properties. Thus, controlling instead of avoiding should be more rational to the concern about its detrimental effect. The control is more achievable in a compositional non-equilibrium and defect-containing microstructural environment. Defects may easily induce local composition segregation and even produce similar atomic arrangements of the precipitate phase that provide structural conditions for their nucleation and growth (Zhao et al., 2022). However, the current research on the effect of defects in this topic mainly focuses on their contribution to atom diffusion to locally achieve the composition criterion, but much less on structural fluctuation. Consequently, an in-depth investigation of the crystal-defect-assisted formation mechanisms is of particular interest for both practical application and theoretical modeling.

Under such a context, the deformation and dislocation-dissociation-assisted formation mechanisms of the sigma phase in a Co-Cr-V MEA ($Co_{66.66}Cr_{16.67}V_{16.67}$) and its impact on microstructural heterogeneity was thoroughly investigated in the present work. The alloy was cold rolled to produce a high density of crystal defects and then heat treated. The defect-associated precipitation process was systematically characterized *in-situ* and *ex-situ* by HEXRD in a macroscopic scale, by SEM-EBSD and -ECCI at the mesoscale and by TEM at the nanoscale. This study provides, on one hand, useful information to deepen the understanding of the formation mechanisms of the sigma phase or the other secondary intermetallic compounds and, on the other hand, practical information for alloy design and treatment design to obtain lamellar heterogeneous microstructures using secondary phase particles.

2. Experiments

2.1. Material fabrication and treatment

The alloy with a nominal composition of $Co_{66.66}Cr_{16.67}V_{16.67}$ was prepared by levitation melting with the pure metals of Co, Cr and V (>99.9 % in purity), and then drop-cast into a copper mold to produce a rectangular ingot with dimensions of 150 mm × 90 mm × 30 mm. To homogenize the microstructure and chemical composition, the cast ingot was further hot rolled at 900 °C to a thickness reduction of 50 % and then heat treated at 1200 °C for 2 h. Then, the alloy was cold-rolled along the longitudinal direction by a thickness reduction of 70 % to create a crystal-defect-containing microstructure. Four cold-rolled samples were heat treated according

to the processes illustrated in Fig. 1 to obtain four different states. Among them, three were heated to 900 °C, 950 °C and 1000 °C, respectively, and quenched into liquid nitrogen immediately after the heating to maintain the heated microstructure. The fourth one was heat treated at 1000 °C for 30 min and quenched into liquid nitrogen to preserve the heat-treated microstructure.

2.2. Characterization of phase transformation and texture

To follow the defect-induced phase transformation during heating in the produced alloy, the cold-rolled and the solid-solution-treated (for comparison) sample sheets with dimensions of 10 mm × 5 mm × 1.2 mm were characterized *in-situ* by HEXRD (High Energy X-ray Diffraction). The *in-situ* HEXRD experiment was performed at P07 beam line of PETRA III synchrotron facility at DESY (Deutsches Elektronen-Synchrotron), Hamburg, Germany. The heat treatments were performed using a dilatometer (DIL 805 from TA Instruments). Fig. 2 shows the geometrical setup of the *in-situ* heating and diffraction measurements under the device coordinate system ($X - Y - Z$) and sample coordinate system ($RD - TD - ND$). The diffraction patterns were recorded in the transmission mode with a 2D detector (Perkin Elmer XRD 1621, 2048 × 2048 in pixel, with a pixel size of 200 μm). The instrument calibration was performed using a standard LaB_6 powder sample (with a thickness of 1 mm in the beam direction). The main experiment parameters of the HEXRD measurement are given in Table 1. During the measurement, the sample was heated by the induction coil, and the temperature was measured using a thermocouple welded on the sample surface. The as-solid solution-treated sample was heated from the ambient temperature (< 28 °C) to 1000 °C at a heating rate of 2 °C/s, then cooled in an argon atmosphere, whereas the as-cold-rolled sample was heated from the ambient temperature (< 28 °C) to 1000 °C at a faster heating rate of 20 °C/s, held at 1000 °C for 30 min, then further heated to 1100 °C and held for another 30 min, and then cooled in an argon atmosphere. The measured 2D diffraction patterns were processed using the FIT-2D (Hammersley et al., 1996) by which the Debye-Scherrer rings were integrated to yield 1D diffraction patterns.

The texture of the cold-rolled sample was measured by HEXRD at P07 beam line of PETRA III, using the same detector and under the same device coordinate system (Fig. 2). The incident beam is 0.7×0.7 mm^2 in size, and the sample to detector distance was 1367 mm. Three complete Debye-Scherrer rings, {111}, {200} and {220}, of the FCC phase were recorded. During the measurements, the complete {111}, {200} and {220} pole figures were measured by rotating the samples around the RD from $-90°$ to $90°$ with an interval of 5° (a total of 37 images were recorded). At each position, the exposure time was set to be 4 s to allow the detector to record sufficient diffraction signals. The orientation density functions (ODFs) and the pole density figures were calculated and plotted, using the ATEX software (Beausir and Fundenberger, 2017). The absorption of the XRD due to thickness changes of the measured samples was corrected, using the SteCa program (Nejati et al., 2021).

2.3. Characterization of microstructure

The microstructure and orientation distribution of the alloy were studied using a field-emission gun (FEG) SEM (Jeol-F100) equipped with an electron backscattered diffraction (EBSD) acquisition camera (Symmetry, Oxford Instruments) and the Aztec online acquisition software package (Oxford Instruments). To achieve the surface quality, samples were mechanically polished with SiC grit papers up to P4000, and then electro-polished in a solution of 10 % $HClO_4$ and 90 % C_2H_5OH at a temperature lower than -10 °C under a voltage of 20 V for 20 s. The EBSD measurements were performed under the beam-controlled mode with several step sizes (2 μm, 1.5 μm, 0.15 μm and 50 nm). The results were analyzed with Aztec Crystal software (Oxford instruments) and ATEX software (Beausir and Fundenberger, 2017).

The chemical compositions of the samples were analyzed by SEM-EDX (Energy Dispersive X-Ray) using an FEG SEM (Carl Zeiss Supra 40) equipped with a Bruker EDX detector (XFlash 6|30) and an online acquisition software (Esprit 2.2). The EDX signals were acquired at 15 kV accelerating voltage and at a working distance of 10mm. The composition was quantitatively measured using the standards of pure Co, Cr, and V (registered MAC standards n° 7478). The measurements were performed in both point mode and mapping mode. To check the composition homogeneity of the samples, composition maps were acquired from different sample areas
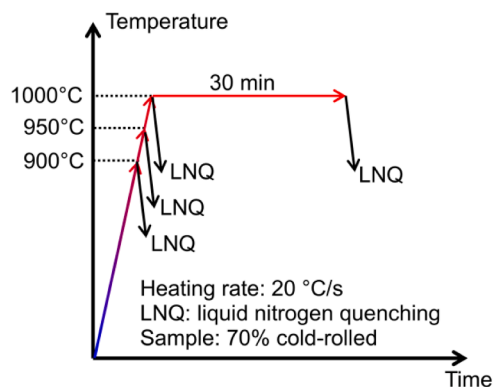

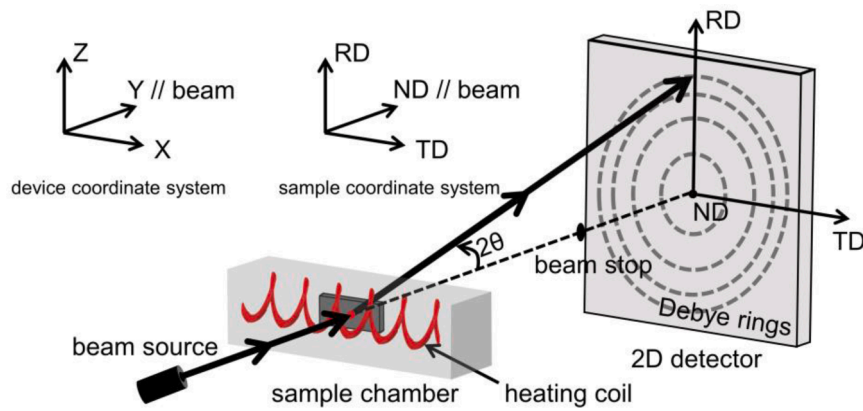**Fig. 1.** Charts of heat treatments applied to cold-rolled samples.

Fig. 2. Experimental set-up of *in-situ* HEXRD measurements. $X - Y - Z$: device coordinate system describing diffraction geometry. RD$-$TD$-$ND: sample coordinate system defined by rolling direction (RD), transverse direction (TD) and normal direction (ND).

Table 1
Experimental parameters and devices of in-situ HEXRD measurement.

Sample	Energy [keV]	Wavelength [Å]	Beam size [mm^2]	Detector distance [mm]	Acquisition time [s]	Detector
Solid solution-treated	103	0.1203	1×1	2094.6	2	Perkin Elmer XRD 1621
Cold-rolled	87.1	0.1423	1×1	1323.3	0.2	Perkin Elmer XRD 1621

each of $225 \times 169 \ \mu m^2$ to ensure a statistical representation. The concentrations of the 3 constituent elements were averaged from the obtained maps. To determine the concentration of the precipitates and the matrix phase, 7 measurements (in point mode) at different locations of the sample were performed. The crystal defects were analyzed by the same SEM, using a backscattered electron (BSE) detector under electron channeling conditions. The same EBSD sample preparation was performed for the EDX analysis and SEM electron channel contrast imaging (ECCI).

The crystal structure of the precipitates and the dislocation configuration and Burgers vectors were examined, using a Philips CM 200 transmission electron microscope (TEM) operated at 200 kV. The TEM is equipped with a LaB6 cathode and a Gatan Orius 833 CCD camera. The thin foils were prepared first by mechanical thinning to 50 μm in thickness and then by electro-polishing to perforation at about $-30\ °C$ with a solution of 10 % HClO$_4$ and 90 % C$_2$H$_5$OH at a voltage of 20 V, using a Struers Tenupol-5 twin-jet electropolisher.

The EBSD diffraction patterns were dynamically simulated and cross-correlated with the experimental ones for crystal structure verification, using the ESPRIT DynamicS software (Bruker)(https://www.bruker.com). The atomic correspondences were analyzed using the CrystalMaker® software(https://www.crystalmaker.com).
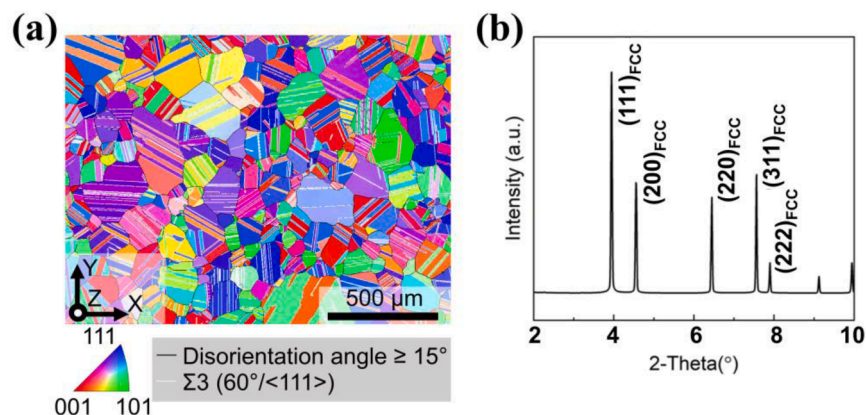

Fig. 3. (a) EBSD X-IPF (inverse pole figure) micrograph and (b) HEXRD pattern of solution-treated sample. X is parallel to prior hot rolling direction.

3. Results

3.1. Solution-treated and cold-rolled states

As evidenced by the EBSD X-inverse pole figure (X-IPF) micrograph and the HEXRD diffraction pattern in Fig. 3, the solution-treated state of the material is composed of a single face-centered cubic (FCC) phase with relatively large equiaxed grains (~120 µm). Almost all grains contain fine plate-shaped annealing twins. In particular, each matrix grain possesses one prevalent twin variant appearing repeatedly with varying thickness, spacing and density.

The EDX analyses results averaged from maps acquired in several areas show that the three constituent elements are distributed homogeneously across the sample, and the concentrations are: Co 65.52±0.16 at%, Cr 16.71±0.06 at% and V 17.76±0.06 at%, respectively, which is in good accordance with the nominal composition. One EDX mapping result is given as an example in Appendix A (Fig. A1).

After the 70 % cold-rolling, the FCC grains are heavily deformed and elongated along the RD direction, as shown in Fig. 4a. Within the deformed FCC grains, two kinds of bands exist, one being thin and oriented at ±25–35° with respect to the RD, as indicated by the white arrows and the other mainly along the RD and with certain thicknesses, as indicated by the yellow arrows. The former should be shear bands formed by dislocation slip, as commonly observed in heavily deformed materials (Huang et al., 2022; Jang et al., 2021). The thick latter ones could be the prior annealing twin plates from the solution-treated state (Fig. 3a). To confirm this, a detailed crystallographic orientation relationship analysis was conducted on these horizontal bands and their neighboring FCC matrices. A representative example is outlined with the white dashed rectangle in Fig. 4a and magnified in Fig. 4b. The {111} direct stereographic projection of all the pixels in the white frame is plotted in Fig. 4b. Although the {111} stereographic projections of the blue grain and the band exhibit widespread, they stay in their respective clusters, suggesting that the two constituent clusters were originated from two distinct orientations. The two blue parts share the same initial orientation. For reference, the average orientation of the blue neighbors and one of its ideal twin orientations were calculated and indicated with the yellow triangles and the black stars, respectively. As expected, the orientation of the band is very close to the indicated twin orientation, confirming that the band was the annealing twin and the blue parts were its matrix. The projection of the twin band shows a much wider spread than that of the blue grain, even though it has much smaller volume. This indicates that during the cold rolling, the twin plates underwent more severe deformation than their matrices. This can also be seen in the magnified micrograph in Fig. 4b where the twin plates were largely fragmented by the cutting through of the thin shear bands. Thus, these twin regions should possess a much higher density of crystalline defects (dislocations, vacancies and boundaries). It should be mentioned that the black strips near the boundaries and the bands are from the EBSD non-indexed pixels. The non-indexation should be due to the poor crystalline perfection of the pixel area and could be regarded as a lattice distortion indicator. Such black strips are always spotted near the severely deformed twin plates. The reason could be such that, on one hand, the twin is deformed by its own dislocation slip under the external loading and, on the other hand, the
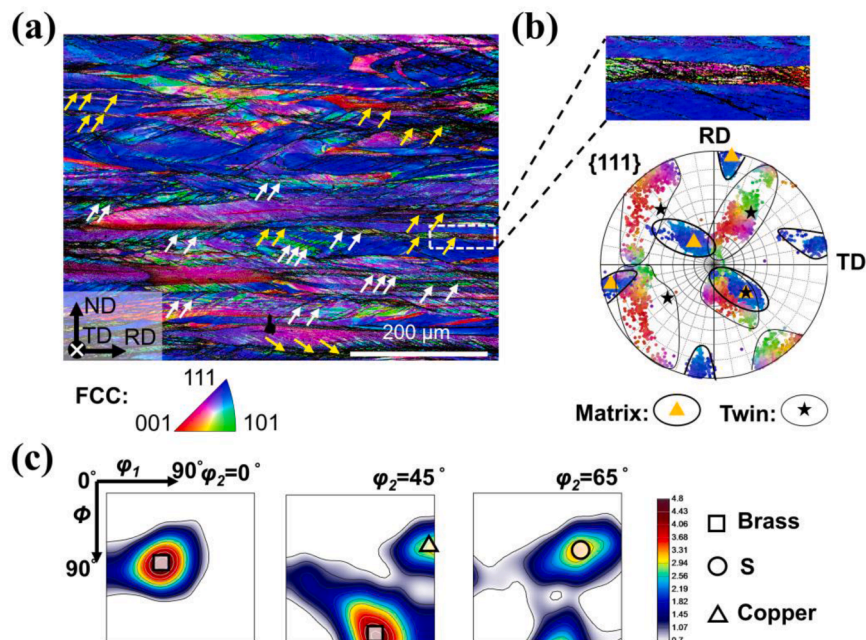

Fig. 4. (a) and (b) EBSD micrographs of 70 % cold-rolled sample where FCC phase is colored according to X-IPF (X//RD) and {111} direct stereographic projections of FCC phase in magnified EBSD micrograph in (b) where poles bear consistent colors in (a) and (b). (c) φ2=0°, 45° and 65° sections of orientation density function (ODF) of cold-rolled FCC phase. White and yellow arrows in (a) indicate deformation bands and deformed twin layers. Black pixels in (a) are non-indexed and serve as crystalline perfection indicators.

dislocations generated in its neighboring matrix will be incorporated into the twin after sufficiently piling-up in front of the twin interfaces, making the twin subjected to additional deformation by the slip transferred from the matrix. This process could be reversed from twin to its neighboring matrix, however, the large number of dislocations generated from the large matrix volumes dominate that the majority of the slip transfer is from the matrix to the twin. The dislocation configuration in the cold-rolled state is shown with the TEM bright field micrograph in Fig. 5a. It is seen that a large number of dislocations were formed by the cold rolling.

The texture of the cold-rolled sample was also measured by the HEXRD and is displayed in Fig. 4c. Clearly, it is composed of three typical rolling components, the Copper, the S and the Brass, indicating that the deformation behavior of the present alloy falls within those of the low stacking fault FCC materials (Kaushik et al., 2021; Sathiaraj et al., 2020a, 2020b; Shankar et al., 2024). Owing to the specific presence of the deformed annealing twins, the cold-rolled microstructure was characterized by a kind of lamellar structure along the RD that is composed of alternatively distributed severely deformed regions and less severely deformed ones.

In addition to the microstructural change of the FCC phase by rolling, a small amount of hexagonal close-packed (HCP) phase in fine lamellar shape with thicknesses of about 20 nm (as shown in the TEM bright field and dark field micrographs in Fig. 5) was induced. The existence of the HCP phase can also be clearly shown by the HEXRD patterns in Fig. 6. Here, the deformation-induced FCC to HCP transformation is a different topic and will not be investigated in the present work.

3.2. Conditional formation of sigma phase during heating

The defect-induced sigma phase formation in contrast to the defect-free state (solution-treated) was further studied by the *in-situ* HEXRD. Fig. 6a and b show the HEXRD patterns of the cold-rolled sample acquired during heating and cooling. During heating up to 700 °C, the HCP phase progressively disappeared. Then, a new phase appeared starting from about 900 °C. The positions of the new peaks resemble those of the so-called sigma phase frequently observed in the Cr containing high entropy alloys (Laplanche, 2020; Lu et al., 2023). When the temperature rose to 1000 °C, the diffraction peaks of the new phase reached the maximum heights. However, when the temperature continued to increase, the peaks started to decrease and almost disappeared at 1100 °C (Fig. 6a). Interestingly, the new phase did not re-appear during the cooling process, even though the heating and cooling were set to the same rate (20 °C/s), as seen in Fig. 6b. This indicates that the formation of the new phase was strictly related to the high density of defects generated by the cold rolling. Indeed, during cooling, the deformed microstructure was already replaced by a recrystallized and defect-free micro-structure (as shown later). To validate this, the *in-situ* HEXRD was also performed from ambient to 1000 °C at a much lower heating rate (2 °C/s) to the solution-treated sample that was fully recrystallized before heating. The spectra in the HEXRD patterns in Fig. 6c clearly demonstrate that during the whole heating process, the FCC phase in the solution-treated (defect-free) sample was very stable. No phase transformation occurred. A careful study of the crystal structure and composition features of this new phase confirms that it is the topographically-close-pack tetragonal sigma phase with much higher Cr and V concentrations with respect to the matrix FCC phase. The details are given in Appendix B. The complete crystal structure data obtained are of vital importance that allow to analyze the correlation between the crystal structure of the sigma phase and the defect features and the macroscopic texture relation with the shear bands formed during the cold-rolling, as detailed later.

Fig. 7a-c shows the EBSD X-IPF (X//RD) micrographs of the cold-rolled sample after isothermal holding at 1000 °C for 30 min to demonstrate the microstructural impact of the formation of the sigma phase. For the FCC phase, it is already fully recrystallized. Interestingly, a lamellar layered structure with bi-modal sized FCC grains (as shown in Fig. 7d) was formed that is quite different from that of the solution-treated microstructure in Fig. 3. Coarse and fine grain layers, as outlined with the dashed yellow lines for the latter in Fig. 7a, are distributed alternatively and stretches along the RD, forming a perfect heterogeneous lamellar structure. For the sigma phase, its presence is also quite heterogeneous in distribution. As seen in Fig. 7b and c, it is in particle shape with a mono-sized distribution and an average size about 1 μm, as shown in Fig. 7e. Globally, the lengths and spacings of the fine grain layer have
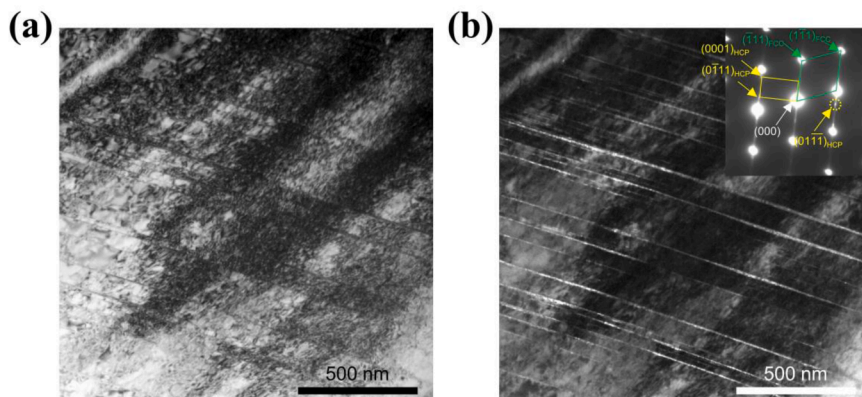

Fig. 5. TEM micrographs of 70 % cold-rolled sample. (a) Bright-field micrograph showing dislocations and (b) dark-field micrograph and selected area diffraction (SAD) pattern. Dark field micrograph was obtained using $(01\bar{1}1)_{HCP}$ reflection (beam // $[110]_{FCC}$), showing a thin lamellar HCP phase.
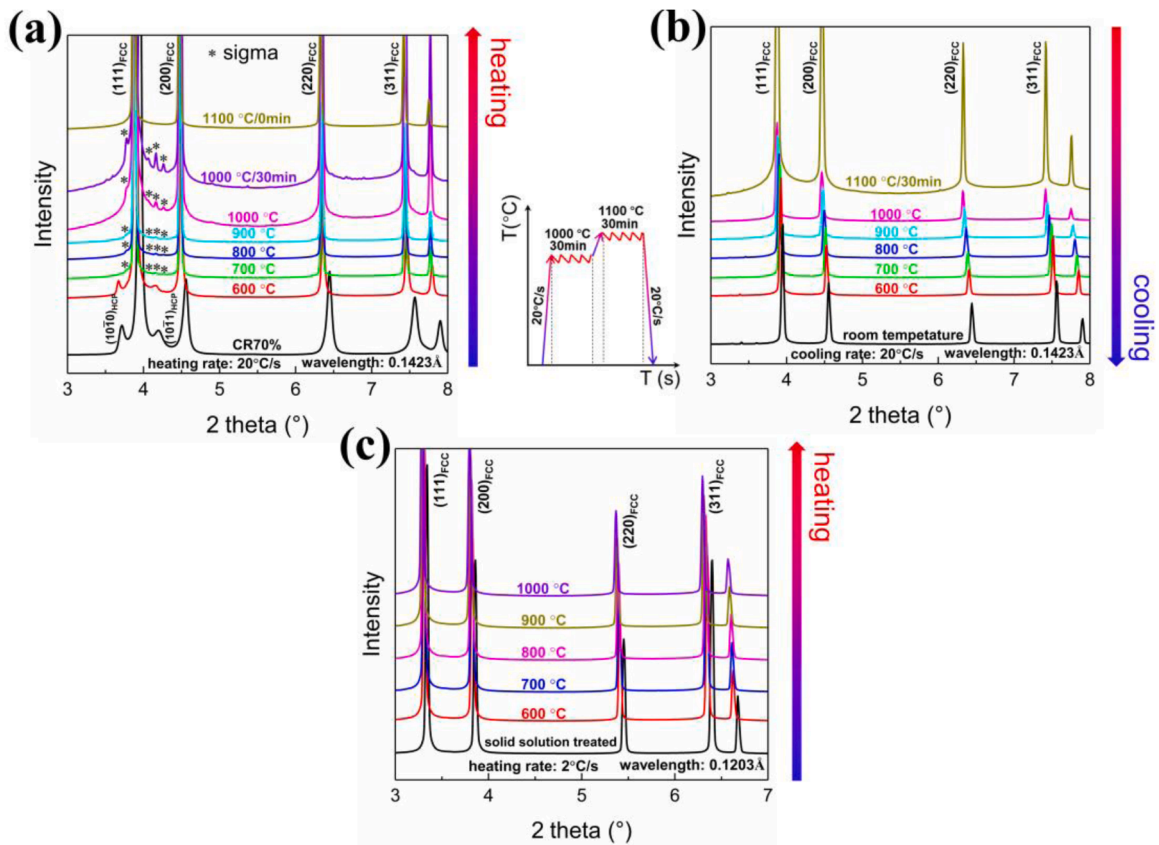
Fig. 6. HEXRD patterns of 70 % cold-rolled sample acquired *in-situ* during (a) heating and (b) subsequent cooling with thermal treatment chart displayed in between. (c) HEXRD patterns of solution-treated sample acquired *in-situ* during heating. Intensity profile of each pattern was obtained by integrating intensity of corresponding 2D Debye-Scherrer rings in a full azimuth angle range.

some coincidences with those of the deformed twins in the cold-rolled state (Fig. 4a and c), inferring that the fine grain layers could mostly be the deformed twin lamellae oriented along the RD.

3.3. Formation process of sigma phase

To unveil the defect-associated formation of the sigma phase, the evolution of the cold-rolled microstructure during heating was investigated. Four cold-rolled samples were, respectively, heated to several specific temperatures at the same heating rate of 20 °C/s as the *in-situ* experiment and then quenched in liquid nitrogen without or with isothermal holding to preserve the microstructures of the heat-treated states. For an easy consultation, the heat treatment chart in Fig. 1 is re-displayed in Fig. 8a.

Fig. 8b-e show the respective global and local characteristic microstructures during heating and heat treatment. The recrystallization features are represented with the EBSD KAM (Kernel Average Misorientation) micrographs, where high KAM level corresponds to the deformed state, whereas the low KAM level to the recrystallized defect free state. When heated to 900 °C, globally, the cold-rolled FCC microstructure features were still preserved (Fig. 8b$_1$, b$_2$ and b$_4$). The features, such as elongated grains, heavily deformed annealing twins, shear bands in the FCC grain interiors (Fig. 8b$_1$ and b$_2$) and the homogeneously distributed high KAM level (Fig. 8b$_4$), are clearly visible, indicating that the recrystallization of the FCC phase did not occur below 900 °C. Locally, the nano-sized sigma particles appeared (as circled with the yellow ellipsoids in Fig. 8b$_3$). The precipitation was not spatially homogeneous. It mainly occurred in the deformed twin band regions and the interface regions (correlation of Fig. 8b$_3$ with b$_2$ and b$_4$) where a large amount of crystal defects existed. Although the precipitates also appeared along the thin intragranular shear bands (Fig. 8b$_3$), the density is much lower with respect to those in the wide boundary regions where black non-indexed (by EBSD) pixels are also very dense (Fig. 8b$_2$ and b$_3$). Indeed, the precipitation was more prevalent in the deformed twin lamellar regions that contained a high density of crystalline defects. When the alloy was heated to 950 °C, recrystallization of the FCC phase occurred, as shown in Fig. 8c$_1$ and c$_4$. Most of the shear bands, prior annealing twin lamellae, and grain boundaries were occupied by small recrystallized FCC grains with low KAM level (Fig. 8c$_4$). Only some isolated prior FCC blocks between intragranular shear bands were still not recrystallized, as seen in Fig. 8c$_1$, and c$_2$ and c$_4$. Such blocks should be less deformed during rolling and possess lower stored energy for recrystallization. The precipitation of the sigma particles continued and was accompanied by very slight coarsening, as shown in Fig. 8c$_3$. However, the inhomogeneous
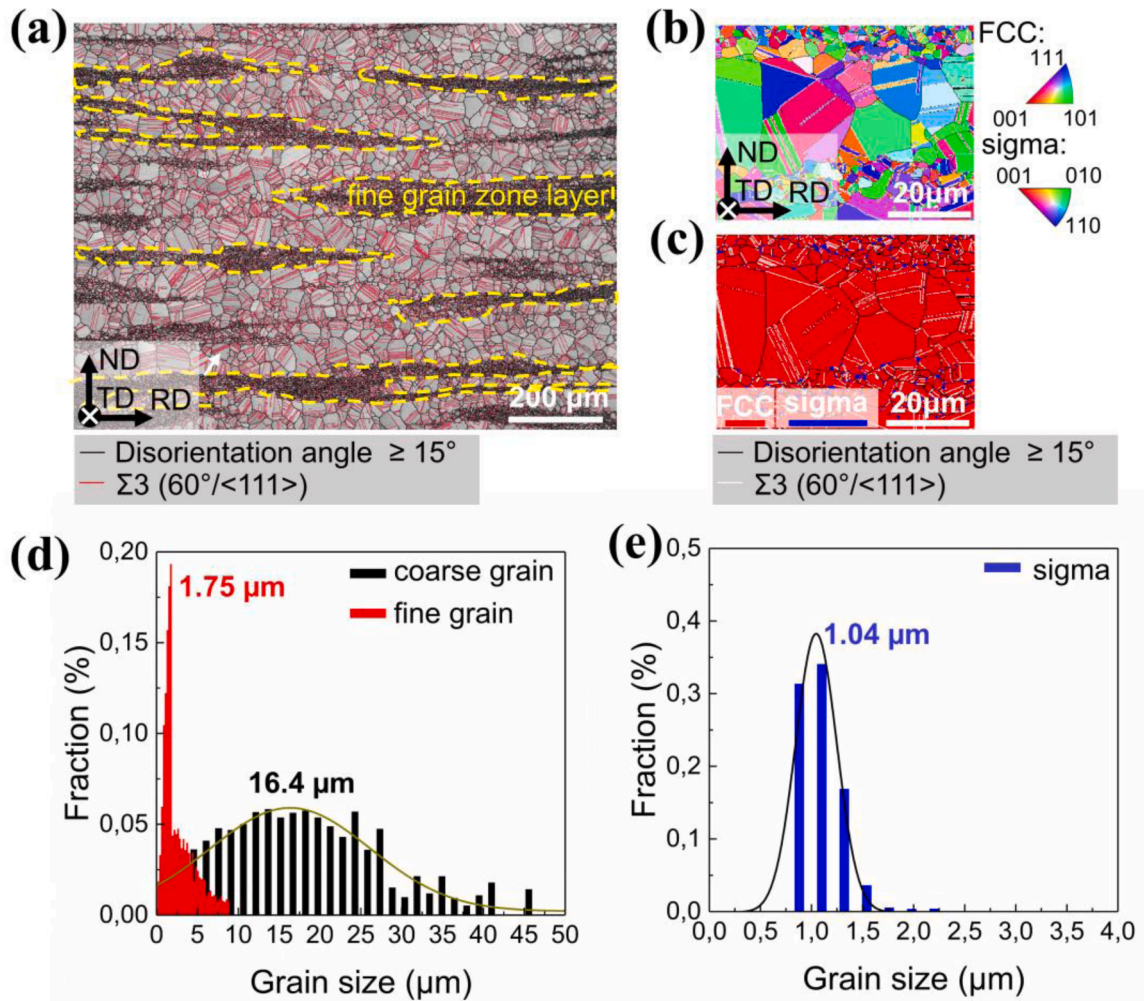
Fig. 7. (a) EBSD Band Contrast (BC) micrograph of sample heat treated at 1000 °C for 30min. (b) and (c) Magnified EBSD phase-indexed micrograph with sigma phase particles densely distributed in fine FCC grain layers. Grain size distributions of (d) FCC grains and (e) sigma phase particles.

spatial distribution remained (Fig. 8c$_3$).

When the temperature reached 1000 °C, the primary recrystallization of the FCC phase was complete, as shown in Fig. 8d$_1$ and d$_4$. Some recrystallized grains even started to grow, as seen in Fig. 8d$_1$. Such grown grains form horizontal strips along the prior RD with a certain spacing. Very locally, the grown grain strips are depleted in the sigma particles and the neighboring fine grains are densely distributed with the particles along the FCC grain boundaries and in the triple junctions, as seen in Fig. 8d$_2$ and d$_3$, inferring that the grains in the zones without or depleted in sigma particles were free to grow, whereas those with densely populated particles were pinned, and their growth was largely impeded and slowed down. Accompanying the primary recrystallization and the subsequent grain growth, the sigma particles started to coarsen but the sizes were still nanometric, as indicated by the yellow arrows in Fig. 8d$_3$. When the sample was held at 1000 °C for 30 min, heterogeneous grain growth was fully developed in the FCC phase, forming the layered structure composed of alternatively distributed fine and coarse grain layers, as seen in Fig. 8e$_1$. Grain growth in the particle-absent layers became very pronounced, whereas that in the particle-enriched layers was still pinned and was very slow. This further enlarged the size difference between the two distinct kinds of layers. In the meantime, the particles became obviously coarsened.

Clearly, the formation of the sigma particles has strong connections with the cold-rolling induced crystal defects. Thus, a close examination of the relation between crystal defects and the sigma particles was conducted, and the results are shown in Fig. 9. Fig. 9a displays the SEM-BSE micrograph and the corresponding EBSD X-IPF (X//RD) micrograph of the sample heated to 950 °C. The matrix FCC grain is in dark (fulfilling the electron channeling condition). The planar crystal defects (thin gray lines), twins and the sigma particles (indicated by the black arrows) are in light gray or white. In the EBSD micrograph, the dark FCC grain and the intragranular twins were well identified; however, the planar defects and the small sigma particles were beyond the EBSD spatial resolution. Further crystallographic analysis using the {111} pole positions (shown in Fig. 9b) of the dark grain evidenced that the planar defects (represented as thin gray lines) are the {111} plane stacking faults. The traces of the four {111} planes are illustrated in the consistent
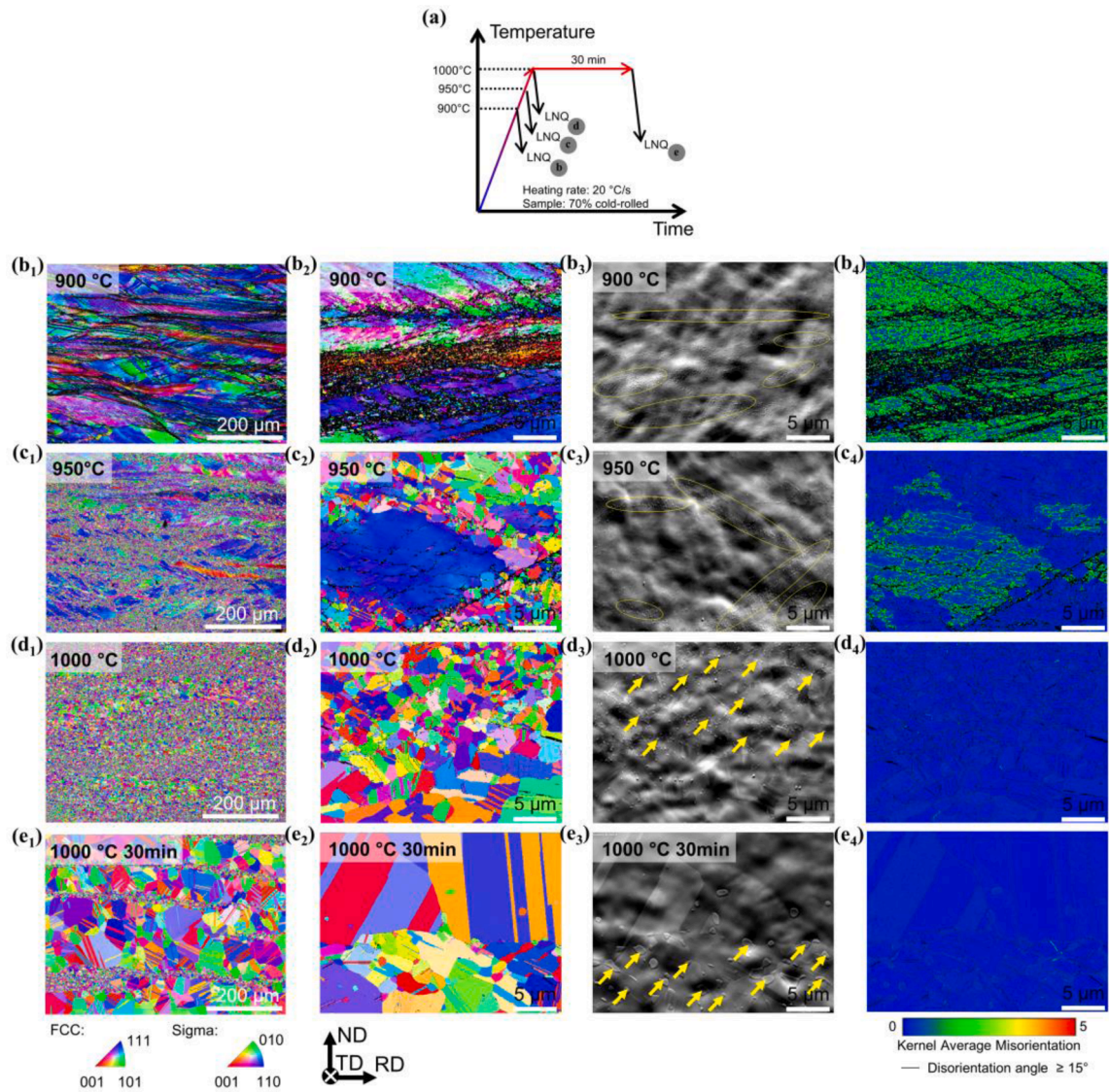
Fig. 8. (a) Heat treatment chart. (b) to (e) EBSD X-IPF (X//RD) micrographs of heat-treated microstructures at global and local scales and corresponding forward scatter electron micrographs of locally scaled EBSD X-IPF (X//RD) micrographs and Kernel Average Misorientation (KAM) micrographs. Yellow circles and yellow arrows indicate dense precipitation zones and precipitates.

colors with those of the {111} poles in the BSE micrographs. It is seen that the sigma particles are all intersected by the stacking faults (Fig. 9a). As an ideal example to show the interaction between the particles and stacking faults, the smallest particle outlined with the yellow frame in Fig. 9a is further magnified in Fig. 9c. It is seen that the particle (outlined with the black dotted circle) is densely intersected by all the four variants of stacking faults, as indicated by the color arrows. In this micrograph the stacking fault characterized by the thickness fringes and represented with the faint gray contrast connecting to the gray lines are visible. Another ideal example to evidence particle-stacking fault connection and the existence of large quantities of stacking faults is shown with the TEM bright field micrograph in Fig. 10. As the FCC phase of this alloys possesses very low stacking fault energy, the dissociation of the dislocations produced by the cold rolling into partials during the subsequent heating is a prevalent phenomenon. This evidence indicates that the unique precipitation of the sigma phase during post-cold-rolling heating is, in a certain way, related to the large number of stacking faults that will be analyzed in the next part.

3.4. Orientation feature of sigma particles

The microstructural examination demonstrated that the formation of the sigma precipitates was more intensive in the severely deformed regions (shear bands, deformed annealing-twin lamella regions). Certainly, such regions contained a large number of crystal
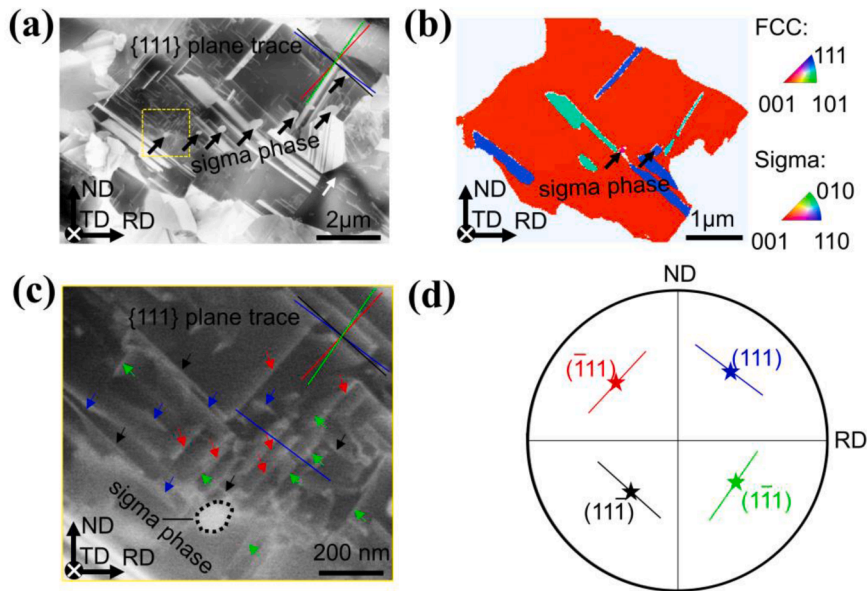
Fig. 9. (a) SEM-backscattered electron (BSE) micrograph of FCC grain fulfilling electron channeling condition and containing sigma particles (indicated by black arrows), annealing twins (in white) and stacking faults (light gray lines with faint thickness fringes). (b) SEM-EBSD X-IPF (X// RD) micrograph of dark grain in (a). (c) Magnified SEM-BSE micrograph of that outlined with yellow frame in (a). (d) {111} pole figure of FCC grain in (b). {111} poles are represented in 4 colors, and their traces are plotted with consistent color lines in (a), (c) and (d) and indicated with consistent color arrows in (c). Sample was heated to 950 °C and immediately quenched.
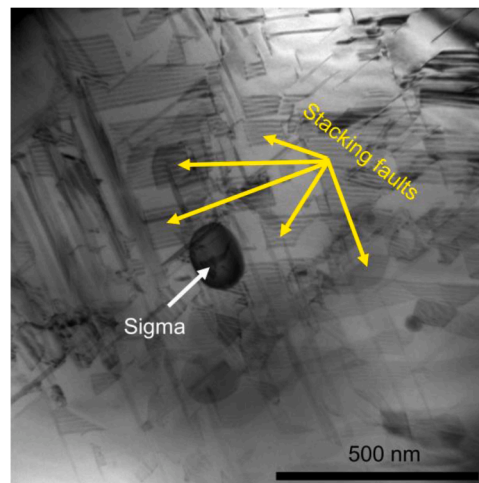

Fig. 10. TEM Bright field micrograph showing a dense population of stacking faults formed during heating to 850 °C and held for 3 min. A sigma particle is surrounded by stacking faults.

defects that are favorable for atom diffusion (Lewis, 1966). However, such highly defective regions may also be helpful for the structure transformation from FCC to tetragonal (Lu et al., 2023). If so, certain crystallographic relations could exist between the two structures. Thus, the textures of the two phases represented with pole figures at different specific heat-treated states were examined.

As already analyzed in Section §3.1, the texture of the cold-rolled FCC phase was composed of three main cold-rolling components, i.e. the Brass, the Copper and the S, as re-shown in Fig. 11a with the {111} pole figure. Surprisingly, the two {111} intensity maxima located at about $20° – 25°$ from the ND toward the $\pm$RD (indicated by the red dash circles in the figure) are clearly in position coincidence with those in the {001} pole figure of the sigma phase, as circled in Fig. 11b$_1$. The orientation data of the sigma phase were extracted from the EBSD data of the fine grain layers, as displayed by the reddish parts in Fig. 11b$_3$ that were obtained after heat treatment at 1000 °C for 30 min. Even though the sigma phase underwent the heat treatment, the coincidence was well preserved. This evidenced that a crystallographic orientation link between the two phases indeed existed, although a perfect orientation relationship expressed with a plane and in-plane direction correspondences was not statistically present. Furthermore, the {111} pole figure of the
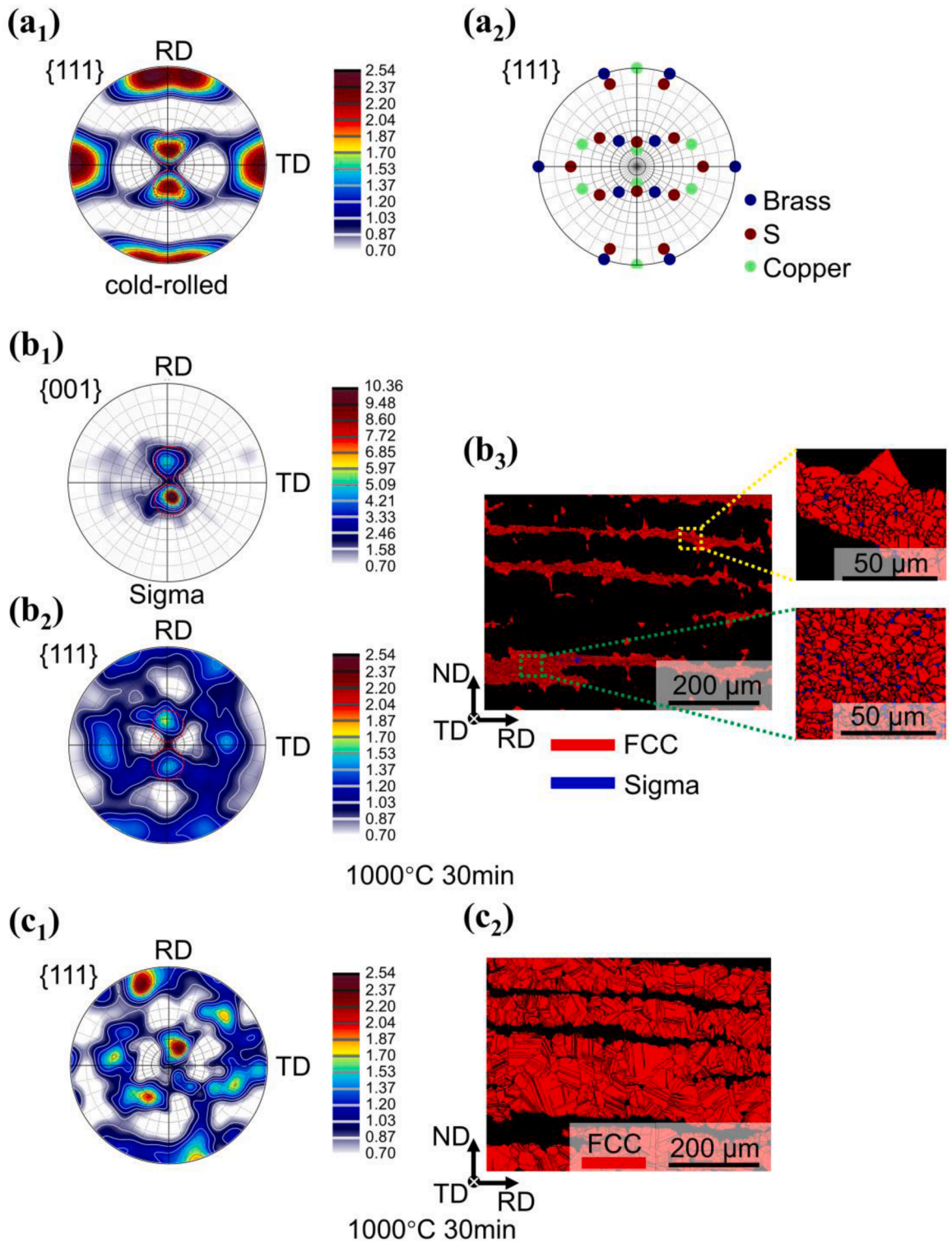
Fig. 11. (a₁) {111} pole figure of 70 % cold-rolled FCC phase measured by HEXRD and (a₂) {111} pole figure of ideal Copper, Brass and S components. (b₁) {001} pole figure of sigma phase and (b₂) {111} pole figure of FCC grains, as well as (b₃) EBSD phase-indexed micrograph of fine grain layers in sample treated at 1000 °C for 30 min. (c₁) {111} pole figure of FCC coarse grains and (c₂) corresponding EBSD phase-indexed micrograph of complementary part to fine grain layers in (b₃).

FCC grains in the fine grain layers in Fig. 11b$_3$ that were neighbors of the tetragonal particles still possessed the two maxima, as circled in Fig. 11b$_2$. For comparison, the {111} pole figure of the complementary coarse FCC grain layers, the red regions in Fig. 11c$_2$, is shown in Fig. 11c$_1$. Large differences can be clearly seen. The two maxima are no longer present and the texture becomes random but dominated by some randomly oriented coarse grains.

Surprisingly, although the texture of the cold-rolled state contained several {111} maxima (those close to the RD and the TD) (Fig. 11a$_1$), only the two close to the ND were "copied" by the {001} of the sigma phase (Fig. 11b$_1$). Thus, we examined the specific texture of the sigma particles with the observed shear bands in the cold-rolled sample through the texture of the cold-rolled FCC phase. To facilitate the analysis, the EBSD band contrast micrograph of the cold-rolled microstructure (from Fig. 4a) and the FCC {111} pole figure (from Fig. 11a$_1$) together with the sigma {001} pole figure (from Fig. 11b$_1$) is re-displayed in Fig. 12. For an easy comparison, the two pole figures are plotted in the sample coordinate system of the EBSD measurement, instead of in the conventional rolling coordinate system as in the previous pole figures. As seen from Fig. 12a, the traces of the intragranular shear bands, as indicated by the white arrows, are oriented at about ±25 to ±35° with respect to the RD in the RD-ND plane. Such shear bands should be made by concentrated dislocation arrays and the traces of the bands correspond either to the parallel shear planes or to stepped shear planes when secondary slip systems were activated (Huang et al., 2022; Jang et al., 2021). In the case of the present FCC phase, the shear planes are the {111} slip planes. Interestingly, these shear band trace orientations coincide with those of the two FCC {111} poles near the ±RD in Fig. 12b, where the average {111} trace of the two poles are plotted with the black solid lines (the angles to the ±RD are also indicated). This means that the dislocations generated by the cold-rolling were majorly located on such {111} planes. Furthermore, these two FCC {111} poles are in perfect coincidence with the sigma {001} poles, as shown in Fig. 12c. This further proves that the dislocations (stacking faults) are indeed at the origin of the non-equilibrium formation of the sigma phase. In this situation, the orientation of the most intensively activated slip planes populated with a large number of dislocations dictated the orientation of the {001} plane of the sigma particles via the FCC {111} to sigma {001} heredity, leading to the specific sigma texture.

4. Discussion

4.1. Formation mechanisms of sigma phase

The compositional (Appendix 2) and crystal structure differences between the present sigma phase and the matrix FCC phase indicate that the precipitation of the sigma phase is diffusional and realized via two different processes: atom diffusion and structure transformation, representing two barriers: compositional and structural.

For the former, the atom diffusion could be achieved by the large number of crystal defects induced by the cold rolling. The high defect density regions favor the segregation of the V atoms that create large lattice distortion due to its large atomic radius (Sohn et al., 2019). In addition, giant shear modulus differences are also generated around the V and Cr atoms (Gao et al., 2013). Thus, the segregation of these two elements in the default regions is energetically favorable. On heating, the dislocations provided favorable channels for the two elements to diffuse and segregate to the severely deformed regions.

Although the composition barrier can be overcome through defect-assisted diffusion, the structural barrier to the transformation should also be overcome, allowing the unique and rapid formation of the sigma phase during the post-deformation heating. Thus, the instant structure transformation having occurred in the present work surely obtained certain 'help' from the crystal defects produced by the cold rolling and their evolution during heating. Using the crystallographic relationship {111}$_{FCC}$//{001}$_{sigma}$ determined between the FCC matrix and the sigma phase (Figs. 11 and 12), an FCC cell that possesses a close atomic correspondence to that of the unit cell of the sigma phase is established and shown in Fig. 13. Clearly, the two cells bear some resemblances but also differences. The resemblances are the cell dimensions. The significant differences are the atomic arrangements. The structure differences, together with the very small diffusion coefficients of the sigma formation elements, like Cr and V, in solid-state explain well why the formation of the
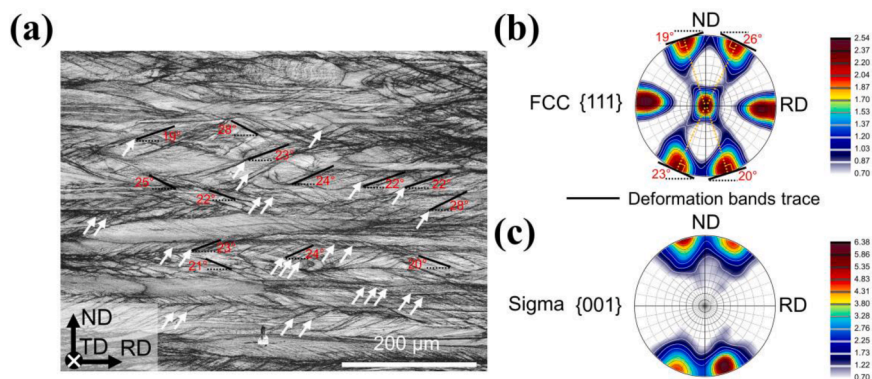

Fig. 12. (a) EBSD band contrast micrograph (same micrograph as in Fig. 4a) and (b) FCC {111} pole figure of 70 % cold-rolled sample. Deformation bands are indicated by white arrows together with their inclination angles with respect to RD. (c) {001} pole figure of sigma phase in sample treated at 1000 °C for 30 min.
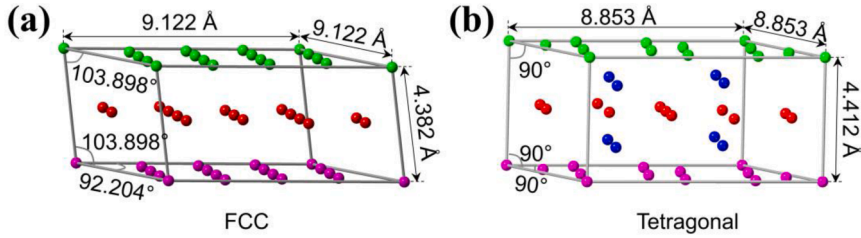
Fig. 13. A cell of FCC phase (a) resembling (b) unit cell of tetragonal sigma structure. Different colors represent different atomic layers.

sigma phase happened uniquely during the post-cold-rolling heating but not in the heating after the solution treatment (defect-free state). In the present work, the formation of the sigma phase is almost instantaneous with the rise of the temperature from the cold-rolled state. Thus, the cold-rolling and the subsequent heating that stimulated intensive dislocation activities should have played a vital role to allow achieving the structural condition for the transformation.

To find out the contribution of the crystal defects, we first picture the detailed structure difference between the two crystals, FCC and topologically close-packed tetragonal. With the orientation link between the two phases (Fig. 12b and c), the two structures can be roughly viewed as a stack of three {111} planes for the FCC matrix and a stack of three {001} planes for the sigma phase, as illustrated in Fig. 14a$_1$ and b$_1$, neglecting the pink and violet layers in the tetragonal structure. It should be mentioned that the different colors used in Fig. 14 are only for distinguishing different {111} FCC planes and different {001} tetragonal planes. There is no correlation with the different element species. The planar spacing of the three {111} FCC planes (4.382 Å) is very close to that of the three tetragonal {001} planes (4.412 Å). This could be the reason why there exists a parallelism between the FCC {111} and the tetragonal {001}. Furthermore, an A/B/A stacking of the three FCC {111} planes makes one more step further toward the tetragonal {001} stacking. Thus, the FCC twin boundaries or the {111} stacking fault provide favorable sites for the nucleation of the sigma phase due to its stacking similarity to the tetragonal structure. This also explains why the sigma particles are always found at the twin boundary regions. Further down to the atomic arrangements of each corresponding FCC {111} plane and tetragonal {001} plane, as shown in Fig. 14a$_2$ and b$_2$, certain similarities and also differences are discernable. If we could just displace the atoms in magenta in plane A of the FCC structure down by ½ of the {111} planar spacing and leave the rest dark blue atoms unchanged on plane A, as shown in Fig. 14a$_2$, the constituent planes A' and B' of the tetragonal sigma should be formed with some slight in-plane adjudgments of the atoms to reach the atomic positions on the tetragonal planes, as indicated in Fig. 14b$_2$. The same operation could work for FCC plane B to form tetragonal planes C' and D' after a clock-wise rotation of 28° around the plane normal. However, the simple collective displacement of the selected atoms seems unrealistic for the structure transformation. The change from the FCC plane A/B to the tetragonal plane A'/C' in Fig. 14a$_2$ and b$_2$ should be achieved via the movement of partial dislocations from the dissociation of the perfect dislocations during the recovery and recrystallization processes.

As illustrated in Fig. 15a, the atomic arrangement of plane A' can be easily achieved by the consecutive movements of $a/6[11\bar{2}]$ and
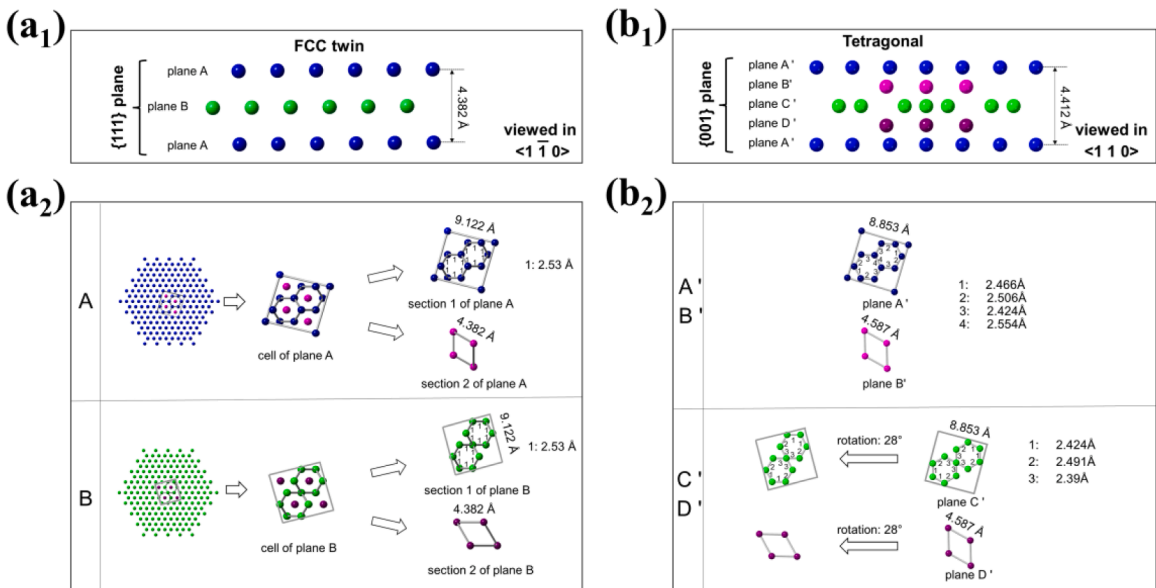

Fig. 14. Detailed structure comparison between FCC and tetragonal sigma phase. (a1) and (b1) FCC A/B/A {111} plane stacking and tetragonal {001} plane stacking. (a2) and (b2) Atomic arrangements on each FCC {111} plane and tetragonal {001} plane.
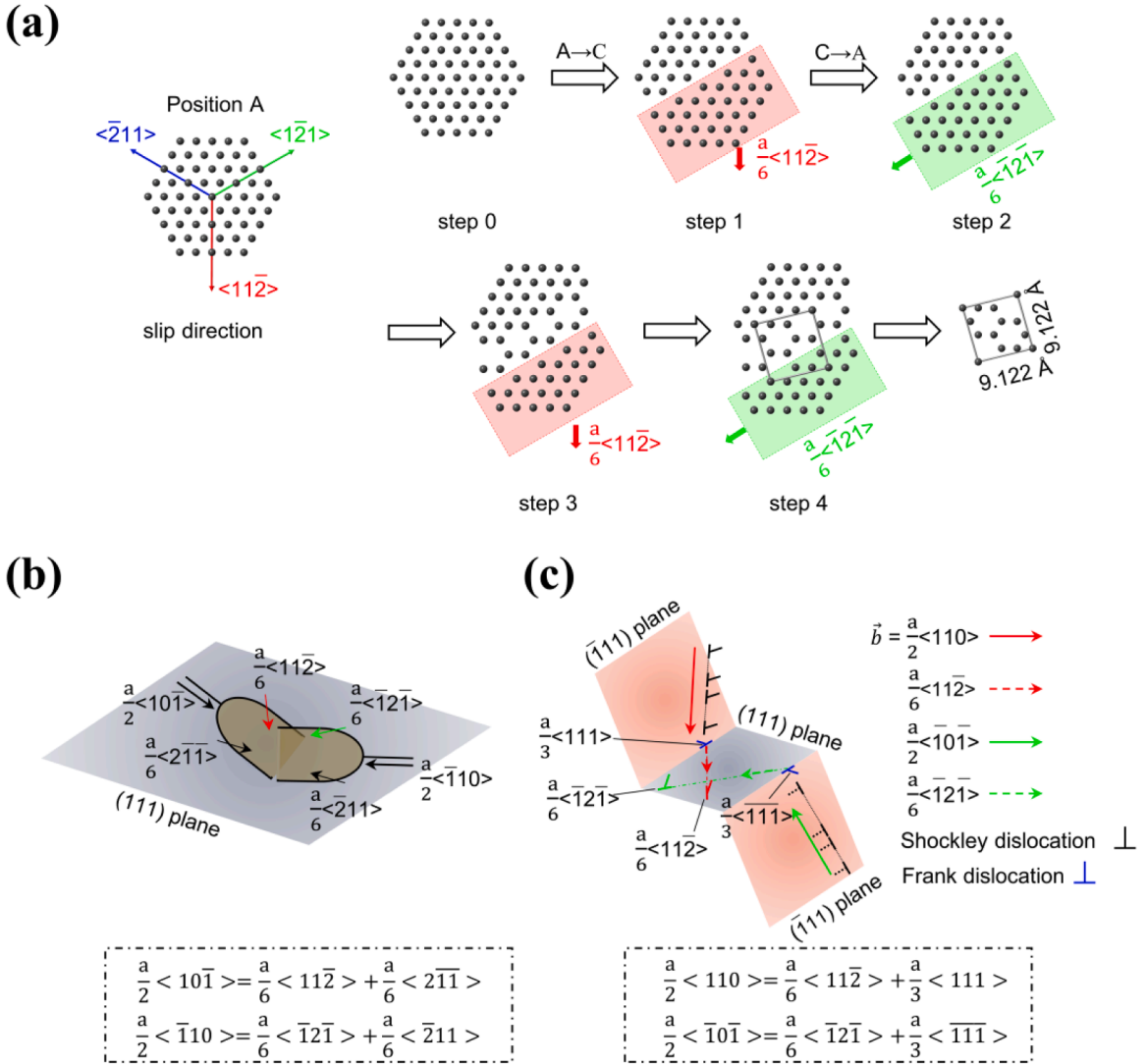
Fig. 15. (a) Illustration of structure transformation from FCC to quasi-tetragonal structure by successive movement of different Shockley partial dislocations (a) and two different mechanisms of dissociation of perfect $a/2\langle110\rangle$ dislocations: co-planar dissociation (b) and cross-slip associated dissociation (c).

$a/6[\overline{1}2\overline{1}]$ Shockley partial dislocations. The operation of the $a/6[11\overline{2}]$ partial dislocation to the atoms shaded in red in step 1 displace these atoms from FCC position A to C, then the operation of the $a/6[\overline{1}2\overline{1}]$ partial to the displaced atoms shaded in green in step 2 displace these atoms from position C to the next A positions. The two steps create a distorted region between the non-displaced and displaced atom zone. Repeating the two steps to the atoms shaded in the second row in Fig. 15a further enlarges the distorted region. The atomic arrangement of this region, as outlined with the gray frame in Fig. 15a, is very close to that of the tetragonal {001} plane. In this way, the {001} tetragonal plane could be rapidly formed from the distorted {111} FCC plane. This transformation path is realistic and can be indirectly evidenced by the microstructure evolution from the cold-rolled state to the recrystallized state. After the cold-rolling, although the microstructure was highly deformed, no deformation twins were observed, indicating that the deformation was achieved by slip of perfect dislocations. Thus, after the cold-rolling, the microstructure should contain high density of perfect dislocations. After recovery and the onset of the recrystallization, a large number of stacking faults and annealing twins were formed, as seen in Figs. 9a and c and 10, demonstrating the intensive dissociation of the perfect dislocations to partial dislocations. The structure transformation aided by the movement of the partial Shockley dislocations can be indirectly proved by the fact that in the present work, the stacking faults were always observed around the sigma particles, especially when the particles were formed at the early stage. As seen in Fig. 9a, the smaller the particles are, the more stacking faults are around the particles.

The dissociation of the perfect dislocations into partial dislocations can be processed in two different ways. One is the dissociation of one perfect $a/2\langle110\rangle$ dislocation into two Shockley partial dislocations on the same slip plane, as illustrated in Fig. 15b. The other is accompanied by a cross-slip of a Shockley partial dislocation on the cross-slip plane and leaving a Frank partial dislocation behind

(Cohen and Weertman, 1963; Liu et al., 2017), as illustrated in Fig. 15c. The dislocation reaction for the coplanar dissociation is:

$$\frac{a}{2}\langle 10\bar{1}\rangle = \frac{a}{6}\langle 11\bar{2}\rangle + \frac{a}{6}\langle 2\bar{1}\bar{1}\rangle,$$

where the perfect dislocations and the two Shockley partial dislocations are on the same {111} plane. The reaction for the cross-slip associated dissociation is:

$$\frac{a}{2}\langle 110\rangle = \frac{a}{6}\langle 11\bar{2}\rangle + \frac{a}{3}\langle 111\rangle,$$

where the perfect dislocations are on the $\{\bar{1}11\}$ planes and the partial dislocations are on the intersected {111} planes.

To achieve the atomic arrangement illustrated in Fig. 15a, a dissociation of two variants of co-planar perfect dislocations $a/2\langle 10\bar{1}\rangle$ and $\langle 110\rangle$ are required, as shown in Fig. 15b. The movement of the partial dislocations $a/6\langle 11\bar{2}\rangle$ and $a/6\langle \bar{1}2\bar{1}\rangle$ could produce the similar atomic arrangements of the {001} tetragonal planes. Similarly, for the cross-slip dissociation, two variants of perfect dislocations $a/2\langle 110\rangle$ and $a/2\langle 10\bar{1}\rangle$ but on separate $\{\bar{1}11\}$ planes are needed, as illustrated in Fig. 15c and the operation of the two Shockley partials could produce a similar atomic arrangement of the {001} tetragonal planes. Moreover, the two Frank partials (in blue in Fig. 15c) possess opposite signs and they attract each other and could move towards each other by climbing. This mechanism will help to form the atomic plane B' or C' in Fig. 14b$_1$. It should be mentioned that to achieve a certain size of the structure modulation from the FCC structure to the tetragonal structure by the two kinds of dislocation dissociations, a series of parallel perfect dislocation arrays are needed. For simplicity, only one pair of dislocation dissociation for either case is illustrated in Fig. 15b and c. As the precipitation of the sigma particles occurred just after recovery and at the onset of recrystallization, a large number of dislocation arrays should exist at this moment. The dislocation dissociation assisted formation of the sigma phase can explain why the precipitation was such ultra-rapid, instantly with the quick heating (20 °C/s). Without this 'help', the structure transformation from the simple FCC structure to the topologically close-packed tetragonal structure only driven by thermal agitation could be very slow, even though the composition condition had already been fulfilled. From the fact that the majority of the sigma particles have their {001} planes align with the major {111} FCC shear plane traces, as evidenced by their pole figures in Fig. 12, the co-planar dissociation is prevalent in the present work.

4.2. Formation of HL microstructure

The precipitation of the sigma particles in the present alloy is significant in producing the heterogeneous lamellar (HL) microstructure (Fig. 7) that is composed of alternatively distributed soft single FCC phased layers and the hard dual-phased, FCC and sigma, layers. The heterogeneous-structure HEAs and MEAs have recently attracted wide attention owing to their excellent strength and ductility combination (Liu et al., 2022; Wu et al., 2015; Zhang et al., 2020a). The heterogeneous lamellar structures are one of the heterogeneous structures and their formation is even more interesting. Thus, the acquisition of their formation conditions is of particular interest for both alloy composition design and treatment process design. The above experimental and analysis results allow to resolve several crucial conditions for the formation of the heterogeneous lamellar microstructure.

From the composition point of view, first, the alloy should contain sigma-prone elements, such as Cr and V with controlled amount. This means that in the equilibrium state no FCC to sigma transformation occurs. Such a composition has two advantages. One is its propensity to form the sigma phase at non-equilibrium composition conditions and the other is that the amount of sigma phase produced by the non-equilibrium transformation should be limited (in the present case: about 1 %) and the particle size should be small (around 1 μm maximum). Secondly, the FCC phase should possess low or even very low stacking fault energy. Thus, twins exist abundantly in the equilibrium state (for example, after annealing) and dislocation dissociation can occur intensively. From the viewpoint of processing, the alloy should be solution-treated to obtain a single FCC phase with relatively large grains (~100 μm) and containing a large number of thin annealing twin lamellae. Then, cold deformation (cold rolling is very effective) should be applied and the deformed alloy should be annealed to the maximum sigma formation temperature to allow the deformed FCC phase to be recrystallized and the sigma phase to be formed. The annealing twin lamellae allow for the production of the alternatively distributed severe deformation zones (deformed annealing twins) and less severe deformation zones (matrices of the annealing twins) along the rolling direction. The severely deformed zones are more favorable in composition and can provide abundant structure transformation 'helpers' (stacking faults and dissociation of perfect dislocations) during recrystallization to facilitate the precipitation of the sigma phase. The intensive precipitation of fine sigma particles in the severely deformed zones inhibited recrystallization and grain growth, especially the latter. In this way, a heterogenous lamellar microstructure with alternative fine dual-phased (FCC + sigma) layers and coarse single-FCC phased layers can be formed.

5. Summary

In this work, the deformation and dislocation dissociation-assisted formation mechanisms of the sigma phase in a ternary non-equiatomic Co-Cr-V MEA (Co$_{66.66}$Cr$_{16.67}$V$_{16.67}$) induced by conventional cold rolling and subsequent annealing and its impact on microstructural heterogeneity were thoroughly investigated through *in-situ* and *ex-situ* characterization techniques. To resolve the sigma formation mechanisms, the phase transformation and the corresponding texture and microstructure evolution were studied by HEXRD in the macroscopic scale, SEM-EBSD and -ECCI in the mesoscale and TEM in the nanoscale.

The alloy possesses low SFE and belongs to the non-sigma MEA family at equilibrium but with a certain propensity to sigma precipitation when V and Cr segregate. When annealed from the cold-rolled state, nano-sized sigma particles were precipitated at the temperatures between the end of recovery and the onset of recrystallization and ultra-rapidly with heating (20 °C/s). The precipitation was spatially inhomogeneous, mainly in the severely deformed regions from the prior annealing twins formed during solution treatment and grain boundaries to deformation bands. The ultra-rapidity of the precipitation was rooted in the segregation of the Cr and V atoms in the severely deformed regions via dislocation-aided diffusion and dislocation dissociation during recovery and recrystallization. The former was due to the large lattice distortion around the V atoms and the giant shear modulus deviation around the V and Cr atoms, that drove the favorable composition segregation around defects. The latter created the crystal structure nuclei for the structural transformation. The crystallographic texture of the sigma phase has been shaped by the orientation of the most intensively activated slip planes populated with a large number of dislocations via the FCC {111} to sigma {001} heredity.

Owing to the spatially inhomogeneous precipitation of the sigma precipitates, a heterogeneous lamellar microstructure was created after the primary recrystallization, composed of alternatively distributed fine dual-phased layers with fine FCC grains and the inter-granular sigma particles and thick single-phased layers with coarse FCC grains.

The present work sheds new light on the dislocation activity assisted formation mechanisms of sigma and on the conditions of creating heterogeneous lamellar microstructure that benefitted from the deformation-induced spatially heterogeneous precipitation of hard secondary phases.

CRediT authorship contribution statement

Luda Wang: Writing – original draft, Visualization, Investigation, Formal analysis, Data curation. **Hai-Le Yan:** Writing – review & editing, Supervision, Resources, Project administration, Conceptualization. **Yudong Zhang:** Writing – review & editing, Supervision, Methodology, Investigation, Formal analysis. **Benoit Beausir:** Writing – review & editing, Supervision, Software. **Weimin Gan:** Writing – review & editing, Investigation, Formal analysis. **Peltier Laurent:** Writing – review & editing, Investigation. **Nathalie Siredey-Schwaller:** Writing – review & editing, Investigation, Formal analysis. **Claude Esling:** Writing – review & editing. **Xiang Zhao:** Supervision, Resources, Funding acquisition. **Liang Zuo:** Funding acquisition.

Declaration of competing interest

The authors declare that they have no known competing financial interests or personal relationships that could have appeared to influence the work reported in this paper.

Acknowledgements

Appendix

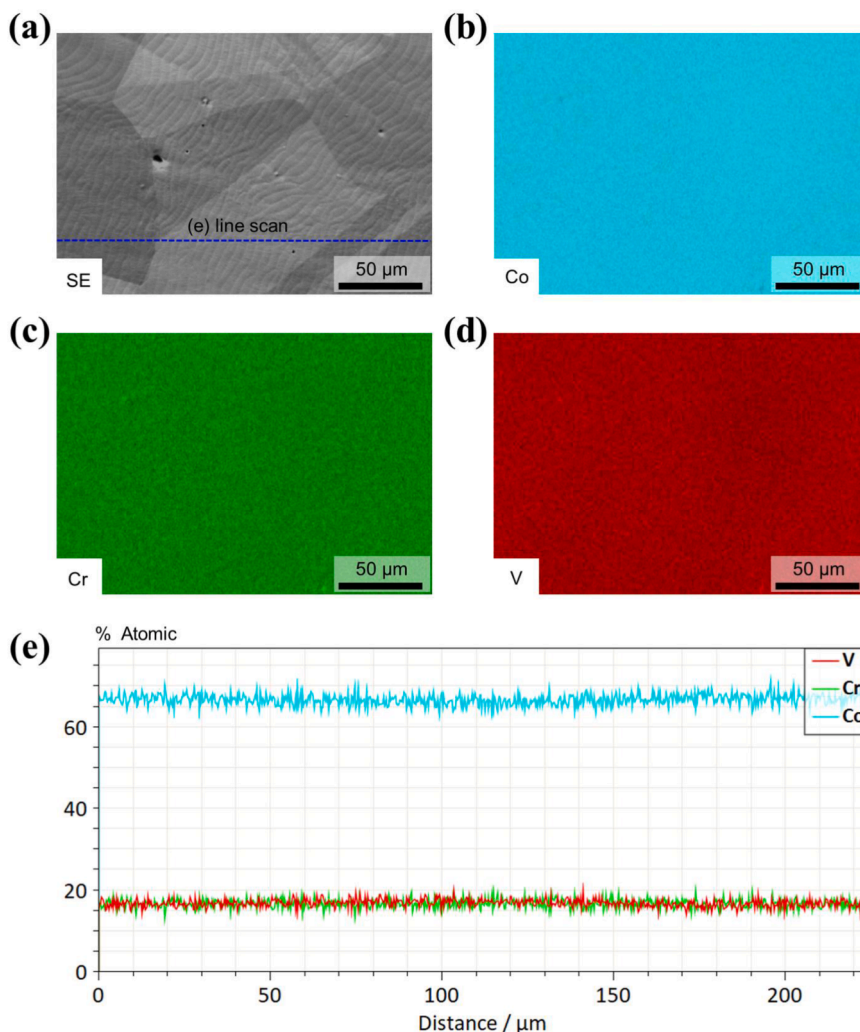### A. EDX result of solution-treated sample
Fig. A1

Fig. A1. EDX results of sample solution-treated at 1200 °C for 2 h (a) SEM secondary electron (SE) micrograph. (b) to (d) Elemental micrographs of same area in (a). (e) Line profiles of 3 elements (V, Cr and Co) from dashed line indicated in (a).

B. Identification of new phase

To obtain the complete information of the precipitates, the chemical composition and the crystal structure were analyzed. Fig. B1a to d show a secondary electron micrograph and its elemental micrographs of a zone in one of the fine FCC grain layers acquired by SEM-EDX. It can be seen that the precipitates are enriched in Cr and V (with the Cr concentration slightly higher by ~2 %) and depleted in Co with respect to the FCC matrix. Quantitative analysis showed that the composition of the FCC matrix ($Co_{65.76\pm0.34}Cr_{16.54\pm0.26}V_{17.7\pm0.16}$) is very close to that of the nominal composition ($Co_{66.66}Cr_{16.67}V_{16.67}$), whereas the composition of the precipitates is $Co_{56.07\pm1.02}Cr_{22.98\pm0.65}V_{20.96\pm0.39}$, as shown in the histogram in Fig. B1e.
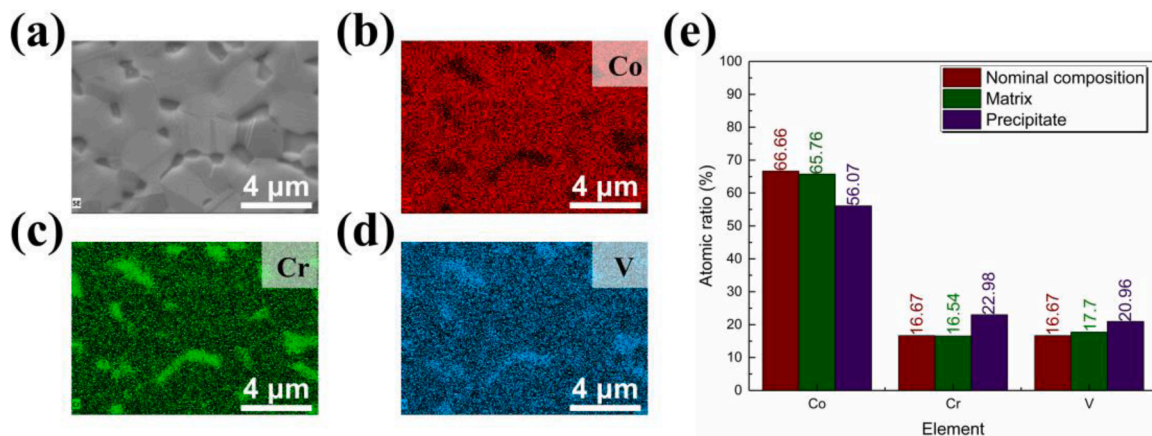
Fig. B1. EDX results of sample heat treated at 1000 °C for 30 min (a) SEM secondary electron (SE) micrograph showing intergranular particles between FCC grains from a fine FCC grain layer. (b) to (d) Elemental micrographs of same area in (a). (e) Histograms of compositions in FCC matrix and new phase, with nominal composition of present alloy as reference.

As the HEXRD diffraction peaks of the new phase are mixed with strong FCC peaks, the crystal structure determination using the HEXRD pattern proved complicated. Thus, we performed TEM and SEM-EBSD electron diffraction analysis, with which we could obtain the single crystal diffraction information of the precipitates. Fig. B2 shows two zone-axis Kikuchi line patterns and the corresponding selected area electron diffraction (SAED) acquired by TEM. The Kikuchi patterns in Fig. B2a and c demonstrate that the crystal structure of the new phase possesses only a 4-fold and a 2-fold rotational symmetry. This symmetry features suggests that the structure could be tetragonal. The TEM-SAED patterns in Fig. B2b and d do not possess any systematic weak super lattice spots. This feature infers that the three constituent elements (Co, Cr and V) are not ordered in the structure. Moreover, the spacings of the lattice planes resolved from the reciprocal lattice vectors of the spots in the SAED patterns are quite large, suggesting that the crystal structure could be represented by a super unit cell. All these indicate that the new phase should be the topologically close-packed sigma phase. Thus, we used the structure model of the sigma phase of CrFe (Bergman et al., 1954) and obtained the lattice constants using the Bragg angles of the HEXRD diffraction peaks of the tetragonal phase. The complete crystal structure information was then obtained and is presented in Table B1. Fig. B3 shows one of the experimental SEM-EBSD Kikuchi patterns of the tetragonal phase and the simulated pattern using the ESPRIT DynamicS (https://www.bruker.com) software and with the refined lattice parameters and the complete atomic positions given in Table B1. The cross-correlation coefficient of the two patterns calculated by the ESPRIT DynamicS (https://www.bruker.com) reached 0.76. This number indicates an excellent match between the two patterns and validates the determined crystal structure of the tetragonal phase. These crystal structure data are very important, with which the precipitates can be identified and their crystallographic orientations be obtained by the EBSD measurements, allowing analyzing the crystallographic orientation link between the precipitates and the matrix FCC phase to resolve their formation mechanism (as detailed later).
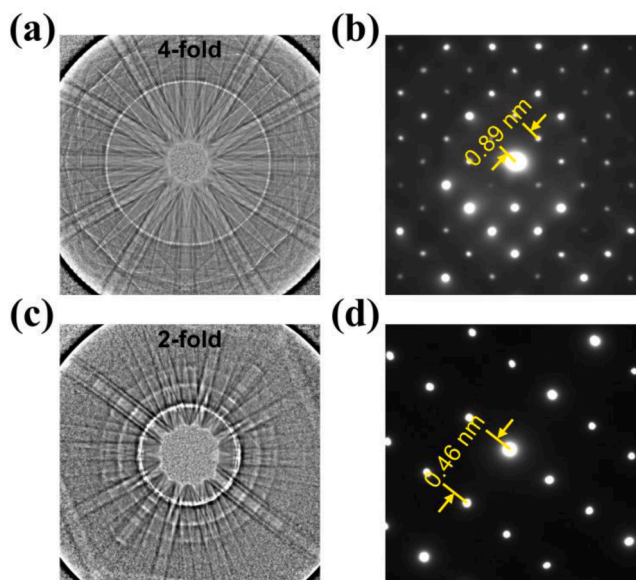

Fig. B2. (a) and (c) TEM Kikuchi patterns and (b) and (d) corresponding selected area electron diffraction (SAED) patterns. Beam direction was parallel in (a) and (b) 4-fold and in (c) and (d) 2-fold rotational symmetry axis of new phase.
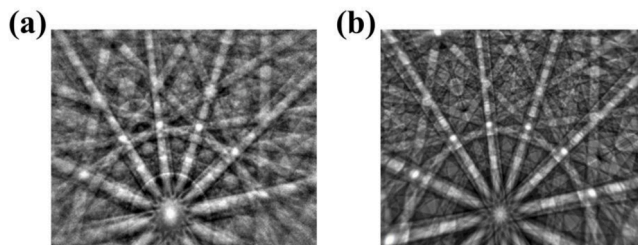
Fig. B3. (a) Experimental EBSD Kikuchi pattern acquired from one of precipitates and (b) dynamically simulated pattern using obtained crystal structure data. Cross-correlation coefficient is 0.76.

Table B1
Detailed crystal structure data of sigma phase.

Crystal system			Tetragonal		
Point group			$P42 / mnm$		
Unit cell formula			$Co_{50}(CrV)_{50}$		
a (Å)			8.8525		
c (Å)			4.4119		
Wyckoff position	Atom	Occupation	x	y	z
2a	Co	0.5	0	0	0
	Cr	0.25			
	V	0.25			
4f	Co	0.5	0.602	0.602	0
	Cr	0.25			
	V	0.25			
8i	Co	0.5	0.868	0.537	0
	Cr	0.25			
	V	0.25			
8i	Co	0.5	0.935	0.262	0
	Cr	0.25			
	V	0.25			
8j	Co	0.5	0.818	0.818	0.748
	Cr	0.25			
	V	0.25			

Data availability

Data will be made available on request.

References

Beausir, B., Fundenberger, J.J., 2017. Analysis Tools For Electron and X-ray diffraction, ATEX - software. Université de Lorraine - Metz. www.atex-software.eu.
Bergman, B.G., Shoemaker, D.P., 1954. The determination of the crystal structure of the σ phase in the iron-chromium and iron-molybdenum systems. Acta Cryst. 7, 857–865. https://doi.org/10.1107/S0365110X54002605.
Chen, X., Liang, Y., Wang, Q., Dong, K., Yang, Y., Feng, S., Zhang, X., Cai, Y., Peng, Y., Wang, K., Kong, J., 2023. Introduction of nanoprecipitation into supersaturated CoCrFeNiMo$_{0.5}$ alloy prepared by laser-powder bed fusion via microstructure tailoring to achieve excellent properties. Scr. Mater. 235, 115636. https://doi.org/10.1016/j.scriptamat.2023.115636.
Cohen, J.B., Weertman, J., 1963. A dislocation model for twinning in f.c.c. metals. Acta Metallurgica 11, 996–998. https://doi.org/10.1016/0001-6160(63)90074-9.
Dong, Y., Lu, Y., Jiang, L., Wang, T., Li, T., 2014. Effects of electro-negativity on the stability of topologically close-packed phase in high entropy alloys. Intermetallics 52, 105–109. https://doi.org/10.1016/j.intermet.2014.04.001.
Fujita, H., Ueda, S., 1972. Stacking faults and f.c.c. (γ) → h.c.p. (ε) transformation in 18/8-type stainless steel. Acta Metallurgica 20, 759–767. https://doi.org/10.1016/0001-6160(72)90104-6.
Gao, M.C., Suzuki, Y., Schweiger, H., Doğan, Ö.N., Hawk, J., Widom, M., 2013. Phase stability and elastic properties of Cr-V alloys. J. Phys. 25, 075402. https://doi.org/10.1088/0953-8984/25/7/075402.
Gourdet, S., Montheillet, F., 2003. A model of continuous dynamic recrystallization. Acta Mater. 51, 2685–2699. https://doi.org/10.1016/S1359-6454(03)00078-8.
Hammersley, A.P., Svensson, S.O., Hanfland, M., Fitch, A.N., Hausermann, D., 1996. Two-dimensional detector software: from real detector to idealised image or two-theta scan. High Press. Res. 14, 235–248. https://doi.org/10.1080/08957959608201408.
He, J., Wu, X., Guo, Y., Makineni, S.K., 2021. On the compositional and structural redistribution during partial recrystallisation: a case of σ-phase precipitation in a Mo-doped NiCoCr medium-entropy alloy. Scr. Mater. 194, 113662. https://doi.org/10.1016/j.scriptamat.2020.113662.
Huang, A.K., Wang, Z., Yuan, Q., Chen, R., Qin, J., Zhang, Y., Liu, W., 2022. Recrystallization behavior of warm rolling and cold rolling Cr-Ti-B Steel during annealing. Metals 12 (7). https://doi.org/10.3390/met12071178.

Hunter, A., Preston, D.L., 2022. Analytic model of dislocation density evolution in fcc polycrystals accounting for dislocation generation, storage, and dynamic recovery mechanisms. Int. J. Plasticity 151, 103178. https://doi.org/10.1016/j.ijplas.2021.103178.

https://www.bruker.com.

https://www.crystalmaker.com.

Jang, T.J., Choi, W.S., Kim, D.W., Choi, G., Jun, H., Ferrari, A., Körmann, F., Choi, P.P., Sohn, S.S., 2021. Shear band-driven precipitate dispersion for ultrastrong ductile medium-entropy alloys. Nat. Commun. 12, 4703. https://doi.org/10.1038/s41467-021-25031-6.

Joubert, J.M., 2008. Crystal chemistry and Calphad modeling of the σ phase. Prog. Mater. Sci. 53, 528–583. https://doi.org/10.1016/j.pmatsci.2007.04.001.

Kaushik, L., Kim, M.S., Singh, J., Kang, J.H., Heo, Y.U., Suh, J.Y., Choi, S.H., 2021. Deformation mechanisms and texture evolution in high entropy alloy during cold rolling. Int. J. Plasticity 141, 102989. https://doi.org/10.1016/j.ijplas.2021.102989.

Laplanche, G., 2020. Growth kinetics of σ-phase precipitates and underlying diffusion processes in CrMnFeCoNi high-entropy alloys. Acta Mater. 199, 193–208. https://doi.org/10.1016/j.actamat.2020.08.023.

Laplanche, G., Berglund, S., Reinhart, C., Kostka, A., Fox, F., George, E.P., 2018. Phase stability and kinetics of σ-phase precipitation in CrMnFeCoNi high-entropy alloys. Acta Mater. 161, 338–351. https://doi.org/10.1016/j.actamat.2018.09.040.

Lewis, M.H., 1966. Precipitation of (Fe, Cr) sigma phase from austenite. Acta Metallurgica 14, 1421–1428. https://doi.org/10.1016/0001-6160(66)90162-3.

Li, J., Wu, Y., Zhang, H., Zhang, X., 2023. Study on the dynamic recrystallization mechanisms tailored by dislocation substructures of a coarse grained Co-free nickel-based superalloy. Mater. Charact. 201, 112961. https://doi.org/10.1016/j.matchar.2023.112961.

Li, L., Li, Z., 2020. Aging induced segregation and nanoprecipitation in a severely deformed equiatomic high-entropy alloy. Mater. Charact. 165, 110369. https://doi.org/10.1016/j.matchar.2020.110369.

Liu, J., Chen, C., Xu, Y., Wu, S., Wang, G., Wang, H., Fang, Y., Meng, L., 2017. Deformation twinning behaviors of the low stacking fault energy high-entropy alloy: an in-situ TEM study. Scr. Mater. 137, 9–12. https://doi.org/10.1016/j.scriptamat.2017.05.001.

Liu, Q., Huang, X.X., Yao, M., Yang, J.F., 1992. On deformation-induced continuous recrystallization in a superplastic Al-Li-Cu-Mg-Zr alloy. Acta Metallurgica et Materialia 40, 1753–1762. https://doi.org/10.1016/0956-7151(92)90118-X.

Liu, W.H., Lu, Z.P., He, J.Y., Luan, J.H., Wang, Z.J., Liu, B., Liu, Y., Chen, M.W., Liu, C.T., 2016. Ductile CoCrFeNiMox high entropy alloys strengthened by hard intermetallic phases. Acta Mater. 116, 332–342. https://doi.org/10.1016/j.actamat.2016.06.063.

Liu, X., Song, K., Kou, Z., Gong, J., Chen, X., Gao, Q., Sun, H., Liu, P., Qu, R., Hu, L., Zhang, Z., Ramasamy, P., Liu, Z., Zhang, Z., Liu, F., Zhang, Z., Eckert, J., 2024. Synergistic grain boundary engineering for achieving strength-ductility balance in ultrafine-grained high-Cr-bearing multicomponent alloys. Int. J. Plasticity 177, 103992. https://doi.org/10.1016/j.ijplas.2024.103992.

Liu, X., Zhang, C., Zhu, C., Vecchio, K., 2022. Creating heterogeneous lamella structure in a multiphase Al-Cr-Fe-Co-Ni complex concentrated alloy. Mater. Sci. Eng. 858, 144150. https://doi.org/10.1016/j.msea.2022.144150.

Lu, W., Guo, W., Wang, Z., Li, J., An, F., Dehm, G., Raabe, D., Liebscher, C.H., Li, Z., 2023. Advancing strength and counteracting embrittlement by displacive transformation in heterogeneous high-entropy alloys containing sigma phase. Acta Mater. 246, 118717. https://doi.org/10.1016/j.actamat.2023.118717.

Ming, K., Bi, X., Wang, J., 2017. Microstructures and deformation mechanisms of $Cr_{26}Mn_{20}Fe_{20}Co_{20}Ni_{14}$ alloys. Mater. Charact. 134, 194–201. https://doi.org/10.1016/j.matchar.2017.10.022.

Nejati, A., Svechnikov, M., Trageser, Wuttke, J., 2021. The stress and texture calculator: data reduction for materials diffraction. https://jugit.fz-juelich.de/mlz/steca-/releases.

Raabe, D., 2014. 23 - Recovery and recrystallization: phenomena, physics, models, simulation. In: Laughlin, D.E., Hono, K. (Eds.), Physical Metallurgy, 5th Edition. Elsevier, Oxford, pp. 2291–2397. https://doi.org/10.1016/B978-0-444-53770-6.00023-X.

Sakai, T., Belyakov, A., Kaibyshev, R., Miura, H., Jonas, J.J., 2014. Dynamic and post-dynamic recrystallization under hot, cold and severe plastic deformation conditions. Prog. Mater. Sci. 60, 130–207. https://doi.org/10.1016/j.pmatsci.2013.09.002.

Sakai, T., Ohashi, M., 1990. Dislocation substructures developed during dynamic recrystallisation in polycrystalline nickel. Mater. Sci. Technol. 6, 1251–1257. https://doi.org/10.1179/mst.1990.6.12.1251.

Sathiaraj, G.D., Kalsar, R., Suwas, S., Skrotzki, W., 2020a. Effect of stacking fault energy on microstructure and texture evolution during the rolling of non-equiatomic CrMnFeCoNi high-entropy alloys, crystals. https://doi.org/10.3390/cryst10070607.

Sathiaraj, G.D., Pukenas, A., Skrotzki, W., 2020b. Texture formation in face-centered cubic high-entropy alloys. J. Alloys Compd. 826, 154183. https://doi.org/10.1016/j.jallcom.2020.154183.

Schwind, M., Källqvist, J., Nilsson, J.O., Ågren, J., Andrén, H.O., 2000. σ-phase precipitation in stabilized austenitic stainless steels. Acta Mater. 48, 2473–2481. https://doi.org/10.1016/S1359-6454(00)00069-0.

Senkov, O.N., Miracle, D.B., 2003. A topological model for metallic glass formation. J. Non Cryst. Solids 317, 34–39. https://doi.org/10.1016/S0022-3093(02)01980-4.

Shankar, G., Gayatri, V., Barrales-Mora, L.A., Suwas, S., 2024. Evolution of recrystallization texture in medium to low stacking fault energy alloys: experiments and simulations. Int. J. Plasticity 172, 103827. https://doi.org/10.1016/j.ijplas.2023.103827.

Shen, X.P., Yao, B.N., Liu, Z.R., Legut, D., Zhang, H.J., Zhang, R.F., 2021. Mechanistic insights into interface-facilitated dislocation nucleation and phase transformation at semicoherent bimetal interfaces. Int. J. Plasticity 146, 103105. https://doi.org/10.1016/j.ijplas.2021.103105.

Sohn, S.S., Kwiatkowski da Silva, A., Ikeda, Y., Körmann, F., Lu, W., Choi, W.S., Gault, B., Ponge, D., Neugebauer, J., Raabe, D., 2019. Ultrastrong medium-entropy single-phase alloys designed via severe lattice distortion. Adv. Mater. 31, 1807142. https://doi.org/10.1002/adma.201807142.

Son, H.W., Hyun, S.-K., 2022. Dislocation characteristics and dynamic recrystallization in hot deformed AM30 and AZ31 alloys. J. Magnesium Alloys 10, 3495–3505. https://doi.org/10.1016/j.jma.2022.04.009.

Tsai, M.H., Chang, K.C., Li, J.H., Tsai, R.C., Cheng, A.H., 2016. A second criterion for sigma phase formation in high-entropy alloys. Mater. Res. Lett. 4, 90–95. https://doi.org/10.1080/21663831.2015.1121168.

Tsai, M.H., Tsai, K.Y., Tsai, C.W., Lee, C., Juan, C.C., Yeh, J.W., 2013a. Criterion for sigma phase formation in Cr- and V-containing high-entropy alloys. Mater. Res. Lett. 1, 207–212. https://doi.org/10.1080/21663831.2013.831382.

Tsai, M.H., Yuan, H., Cheng, G., Xu, W., Jian, W.W., Chuang, M.H., Juan, C.C., Yeh, A.C., Lin, S.J., Zhu, Y., 2013b. Significant hardening due to the formation of a sigma phase matrix in a high entropy alloy. Intermetallics 33, 81–86. https://doi.org/10.1016/j.intermet.2012.09.022.

Wu, X., Yang, M., Yuan, F., Wu, G., Wei, Y., Huang, X., Zhu, Y., 2015. Heterogeneous lamella structure unites ultrafine-grain strength with coarse-grain ductility. Proc. Natl. Acad. Sci. 112, 14501–14505. https://doi.org/10.1073/pnas.1517193112.

Yang, Q., Yan, D., Zhang, Y., Gan, K., Li, Z., 2024. Formation mechanisms of two types of sigma phases and the effects on mechanical behavior in a quaternary metastable high-entropy alloy. Mater. Sci. Eng. 894, 146224. https://doi.org/10.1016/j.msea.2024.146224.

Zhang, C., Zhu, C., Cao, P., Wang, X., Ye, F., Kaufmann, K., Casalena, L., MacDonald, B.E., Pan, X., Vecchio, K., Lavernia, E.J., 2020a. Aged metastable high-entropy alloys with heterogeneous lamella structure for superior strength-ductility synergy. Acta Mater. 199, 602–612. https://doi.org/10.1016/j.actamat.2020.08.043.

Zhang, H., Ou, X., Ni, S., Song, M., 2020b. Toughening alpha-Ti by dislocation-induced phase transformation at crack tips. Mech. Mater. 151, 103629. https://doi.org/10.1016/j.mechmat.2020.103629.

Zhang, H., Wei, B., Ou, X., Ni, S., Yan, H., Song, M., 2022. Atomic-scale understanding of the reversible HCP↔FCC phase transition mechanisms at {10-11} twin tip in pure titanium. Int. J. Plasticity 156, 103357. https://doi.org/10.1016/j.ijplas.2022.103357.

Zhao, P., Xie, G., Chen, C., Wang, X., Zeng, P., Wang, F., Zhang, J., Du, K., 2022. Interplay of chemistry and deformation-induced defects on facilitating topologically-close-packed phase precipitation in nickel-base superalloys. Acta Mater. 236, 118109. https://doi.org/10.1016/j.actamat.2022.118109.